Supplementary Information File for:

A 3D polymorphic Cu-based ultramicroporous MOF capable of CO_2 Uptake and Conversion

by

Mariangela Oggianu,[a] Fabio Manna,[a] Virginia Guiotto,[b] Valentina Crocellà,[b] Valentina Mameli, [a] Carla Cannas, [a] Santiago Quesada,[f,g] Daniele Sassone,[f] Adriano Sacco,[f] Irene I. Gallo Stampino,[d] Raiana Tomazini de Oliveira,[d] Santiago Capelo,[d] Jose Ramon Galan-Mascaros,[d,e] Norberto Masciocchi,[c*] Maria Laura Mercuri[a]*

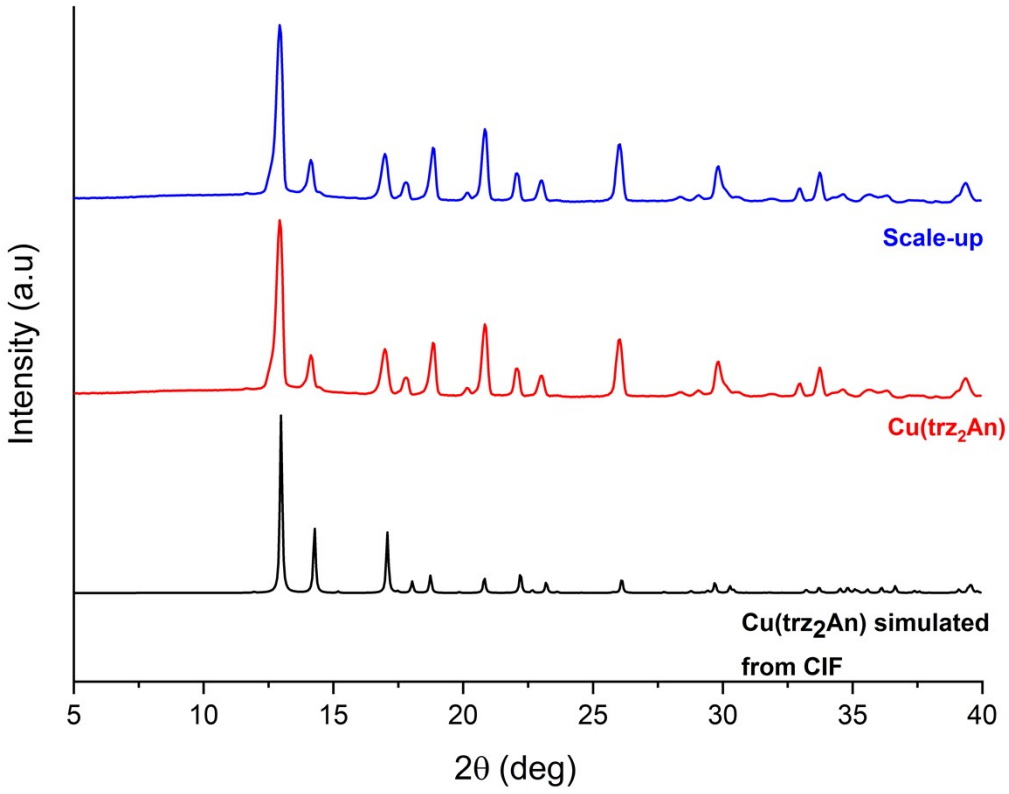

Figure S1. Experimental XRPD patterns of *o*-[Cu(trz_2An)] compared with that calculated from the CIF file after removing the water molecules.

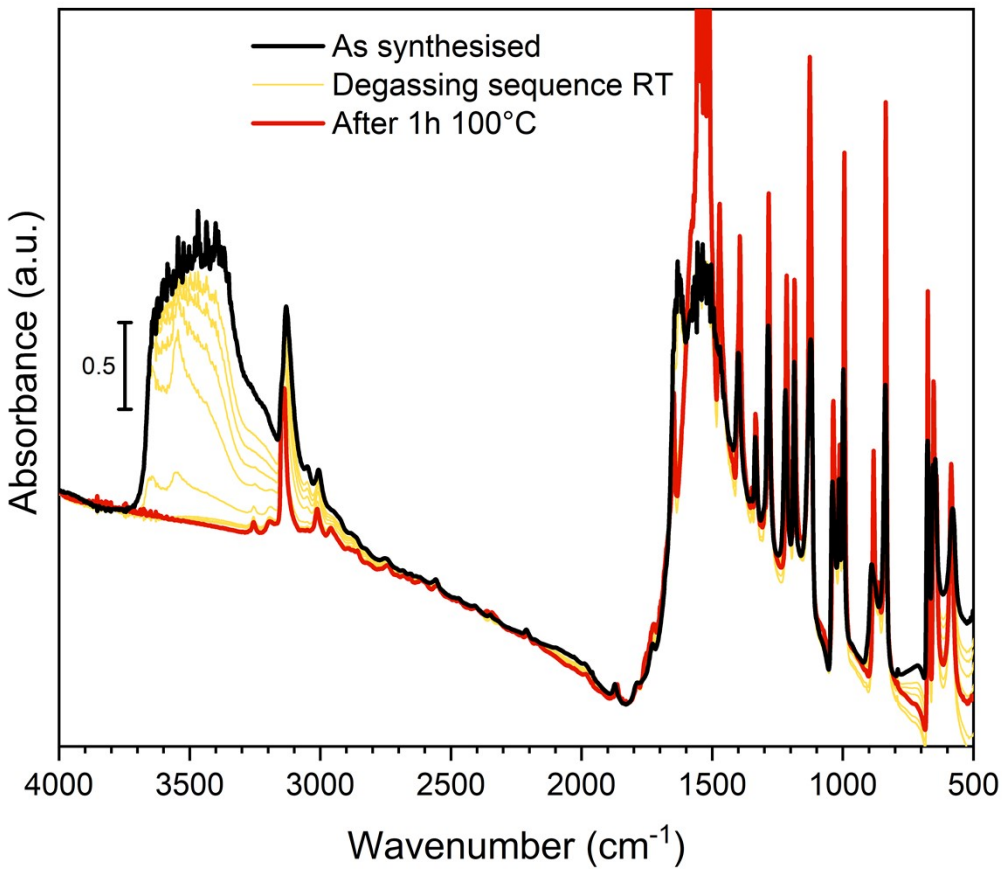

Figure S2. *In situ* IR spectra of [Cu(trz_2An)] during the activation process. The spectrum of the as-synthesized material is shown in black, those of the outgassing sequence at room temperature in yellow and that of completely activated material after 1h at 100°C in vacuum in red.

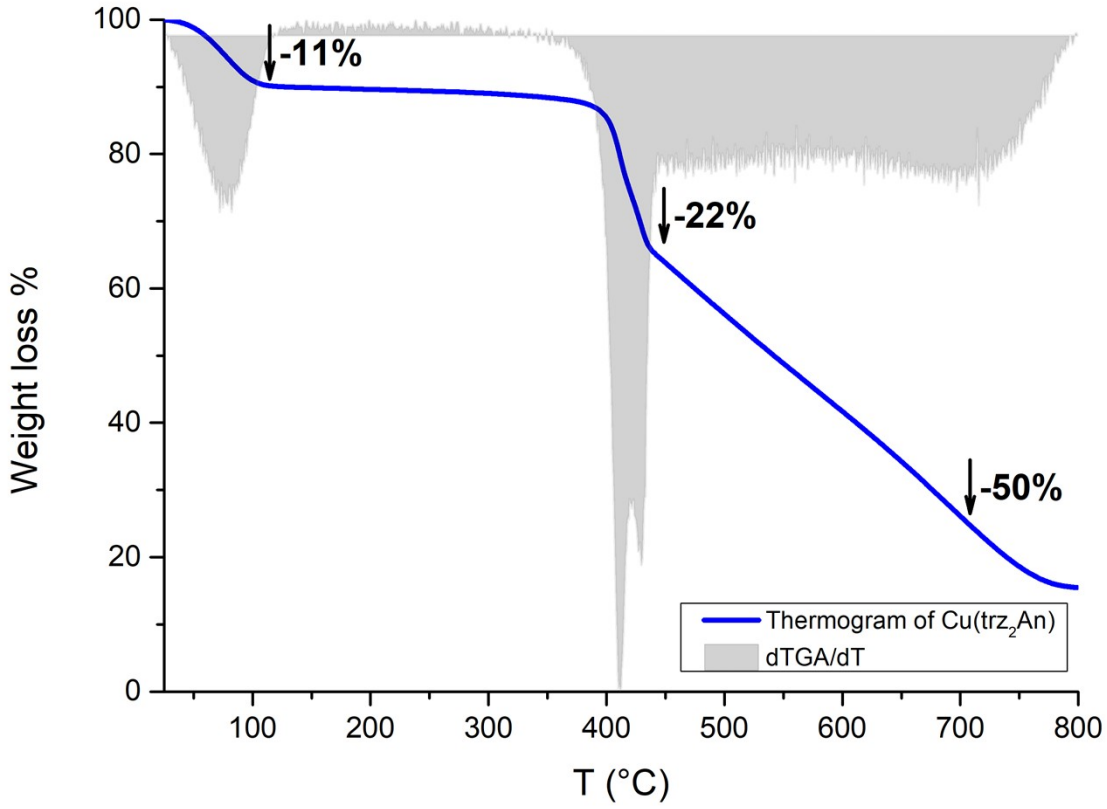

Figure S3. TGA trace of $[Cu(trz_2An)]\cdot nH_2O$. The observed weight loss of 11% corresponds to n = 2.3

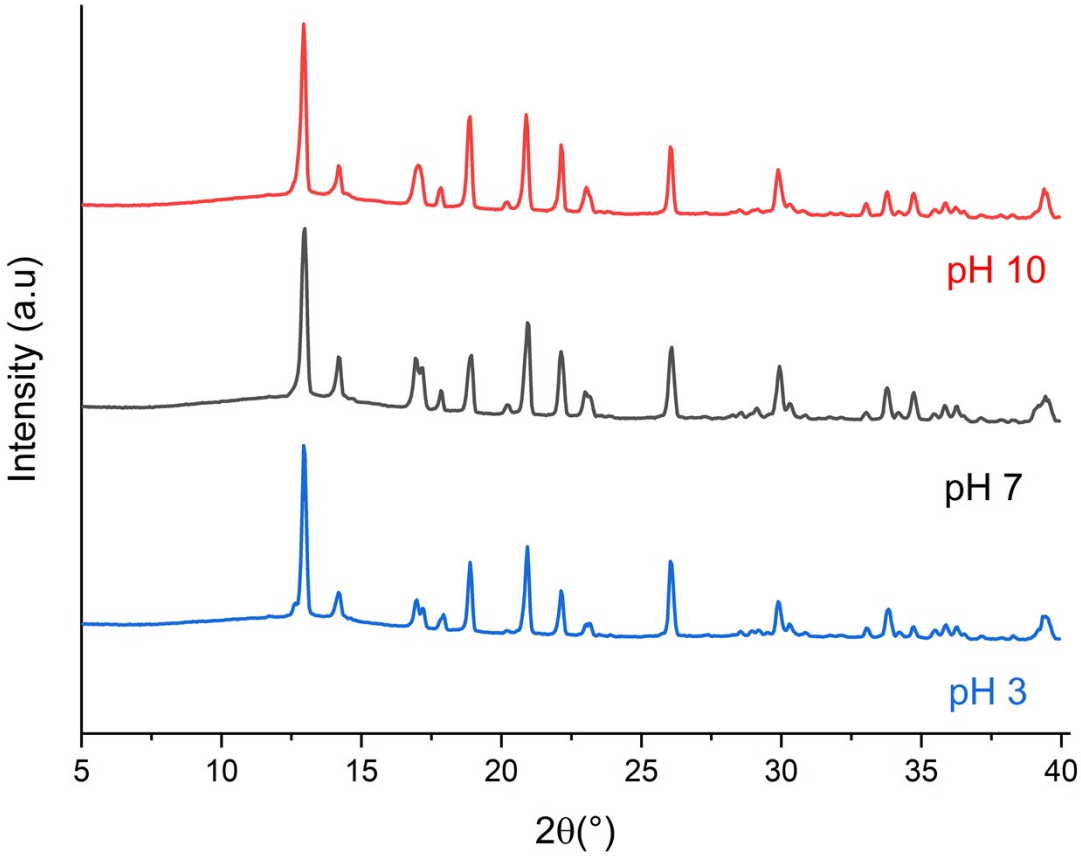

Figure S4. Crystal phase stability of [Cu(trz_2An)], measured by XRPD after soaking the powders in pH-controlled environments.

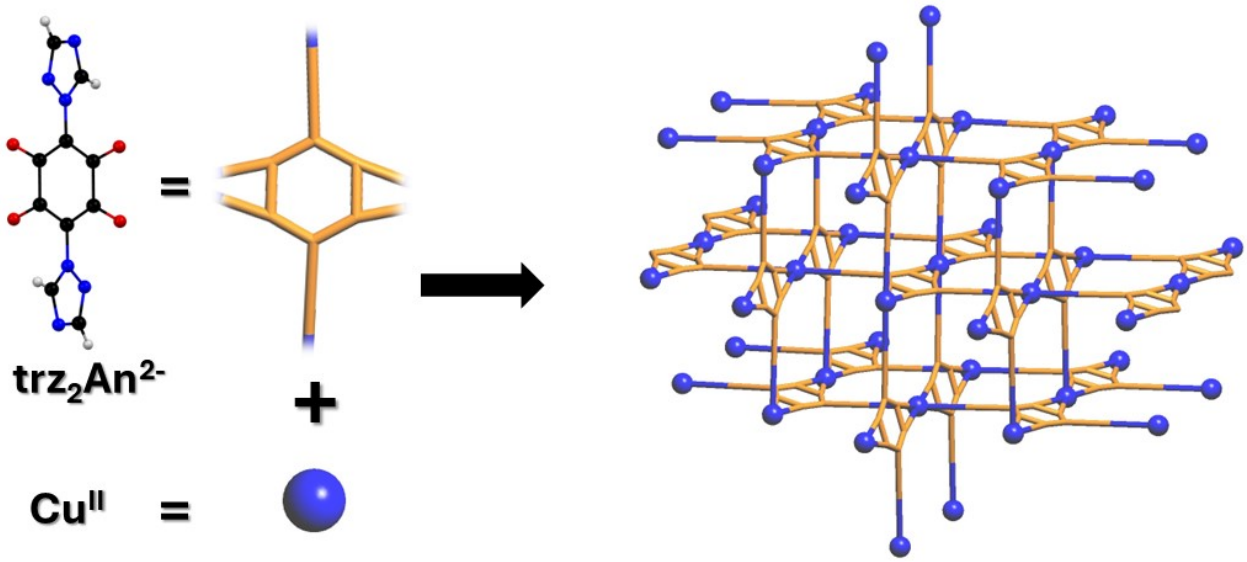

Figure S5. A sketch of the **cds** topology of [Cu(trz_2An)]. The topologies of both monoclinic and orthorhombic [Cu(trz_2An)] phase coincide.

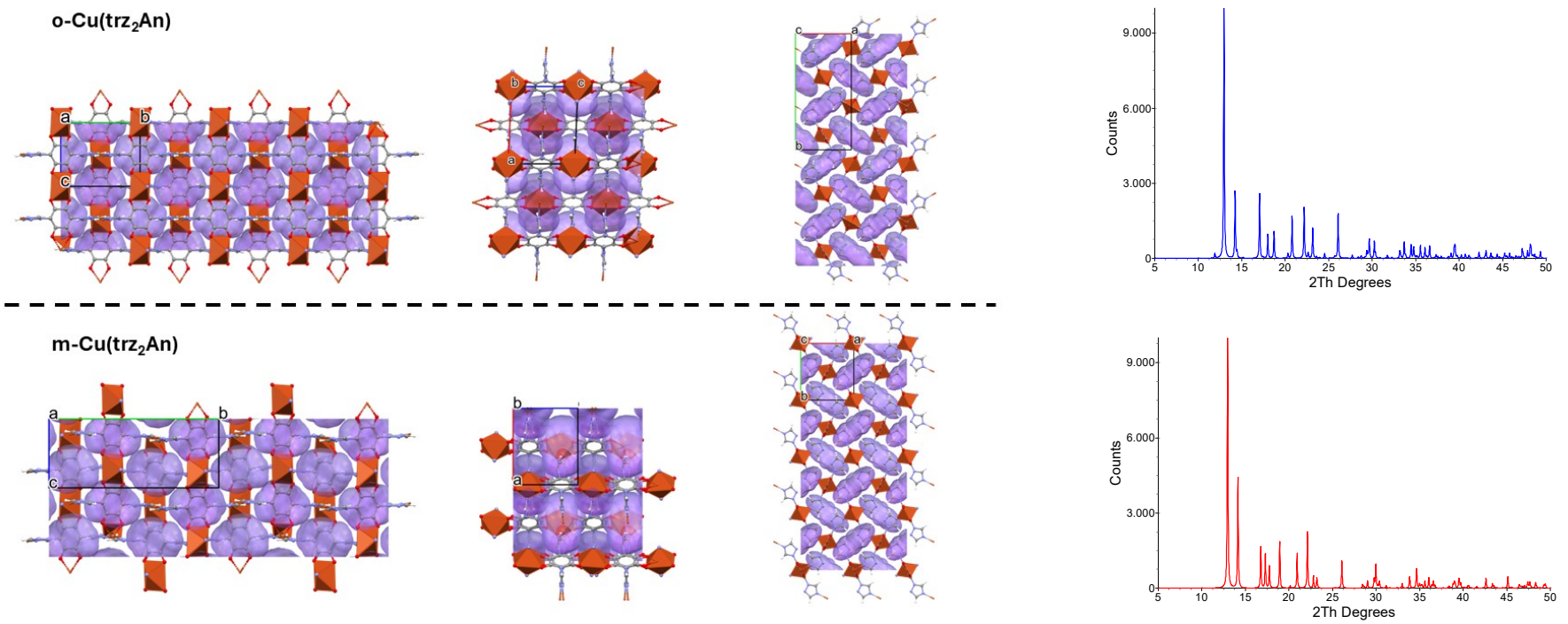

Figure S6. Void shapes and location, calculated from the complete structural models once water molecules are removed, are portrayed by magenta surfaces. In the right panels, the theoretical XRPD traces of the two polymorphs, computed for Cu Kα radiation from the deposited CIF files and equally scaled to a maximum intensity value of 10000 cts.

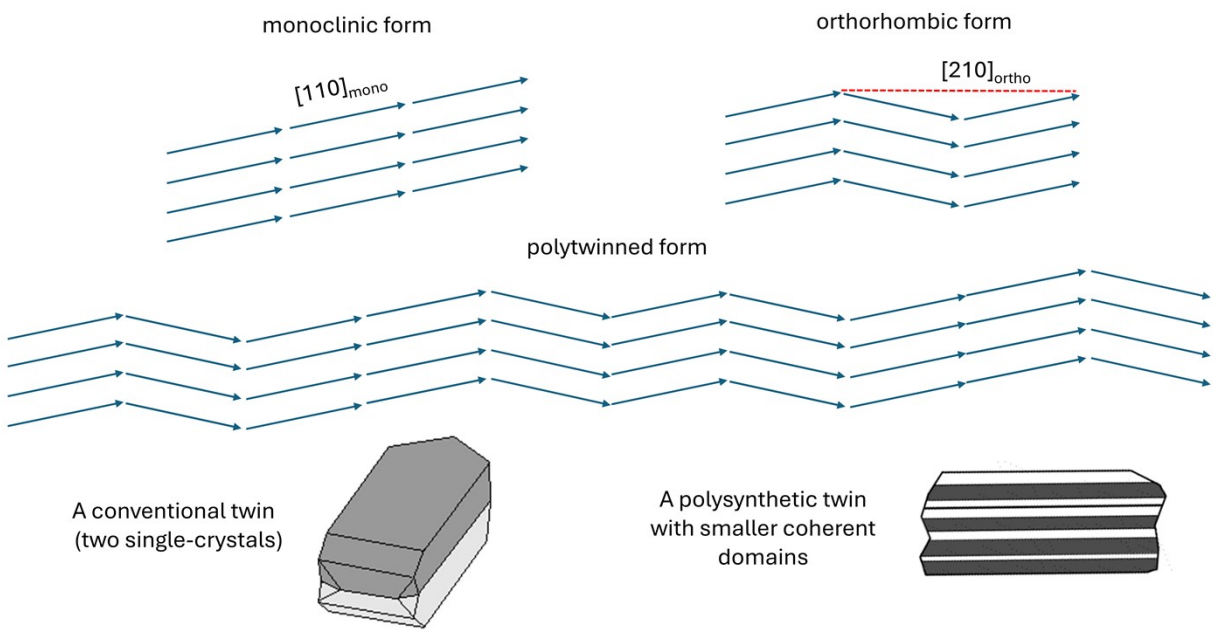

Figure S7. Schematics of the crystal packing of the two [Cu(trz_2An)] polymorphic phases, the 1.7° tilt being exaggerated to 12° for clarity. Top: orientation of the organic ligand in single-crystalline monoclinic (1.7°, left) and orthorhombic (±1.7°, right) forms. Arrowheads do not imply ligand polarity, as they are just a guide to the eye. The polytwinned sequence is also shown, jointly with sketches of *conventional* and *polysynthetic* twins.

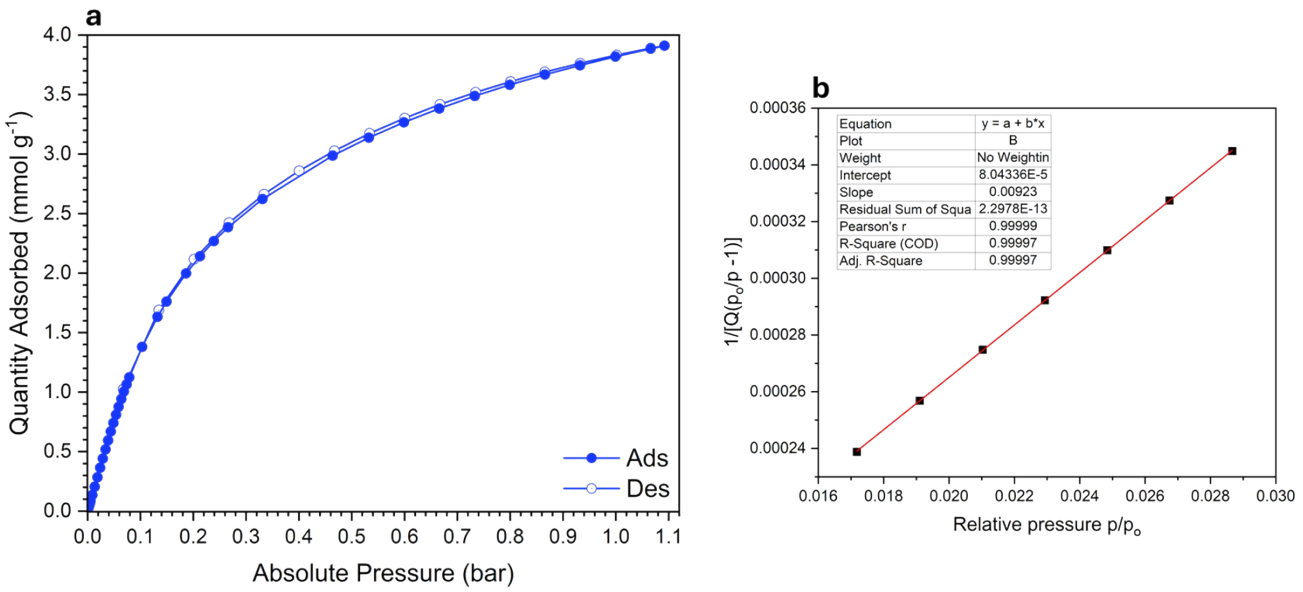

Figure S8. a) CO_2 adsorption/desorption isotherm collected on [Cu(trz_2An)] at 0°C. b) BET equation fit.

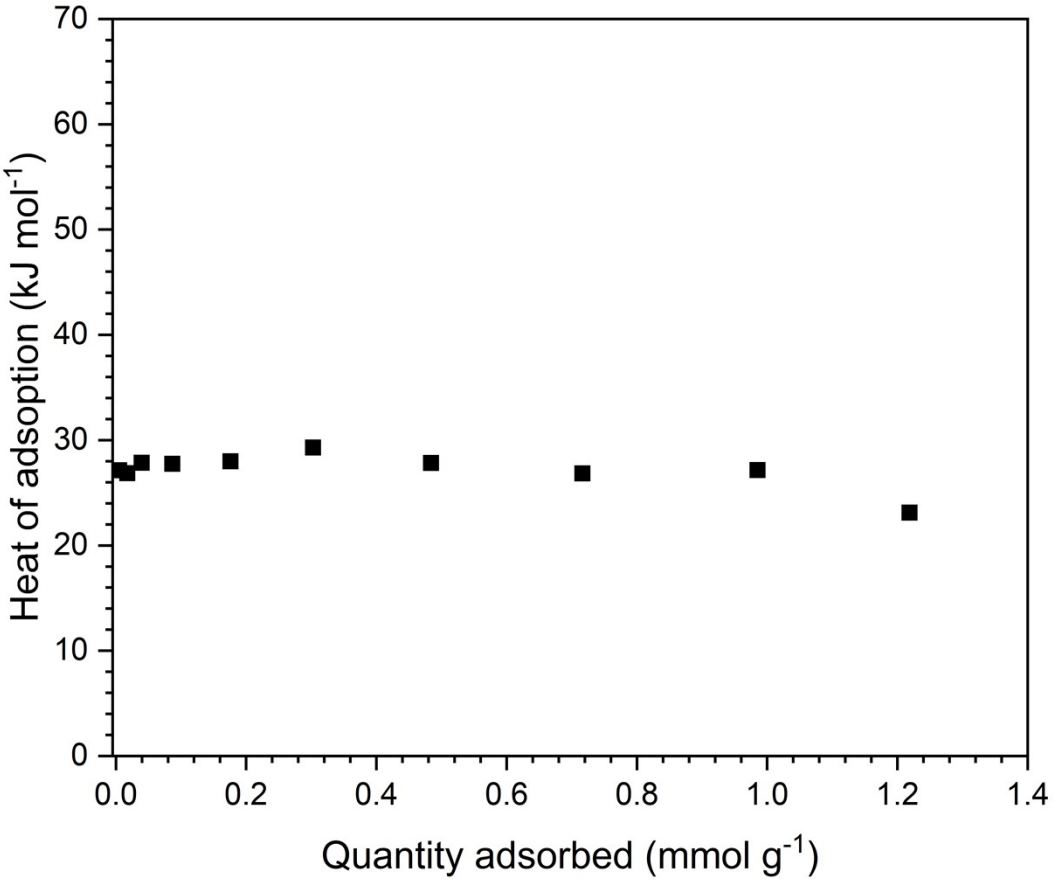

Figure S9. Differential molar heat related to the adsorption of CO_2 on [Cu(trz_2An)] at 30°C

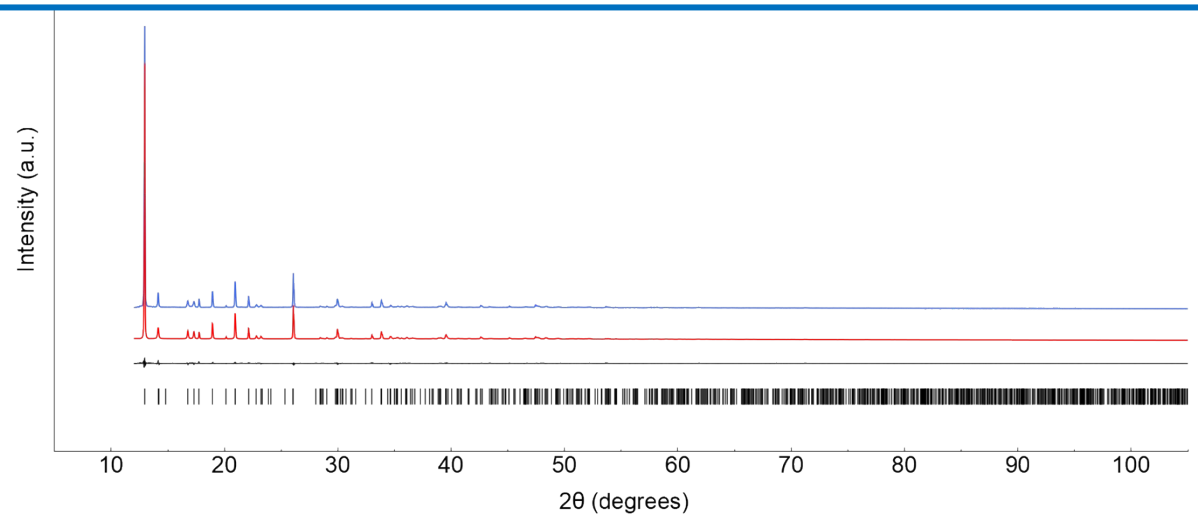

Figure S10. Rietveld refinement plot for *m*-[Cu(trz_2An)]·$3H_2O$. Observed and calculated patterns in red and blue, respectively. Difference plot and peak markers at the bottom.

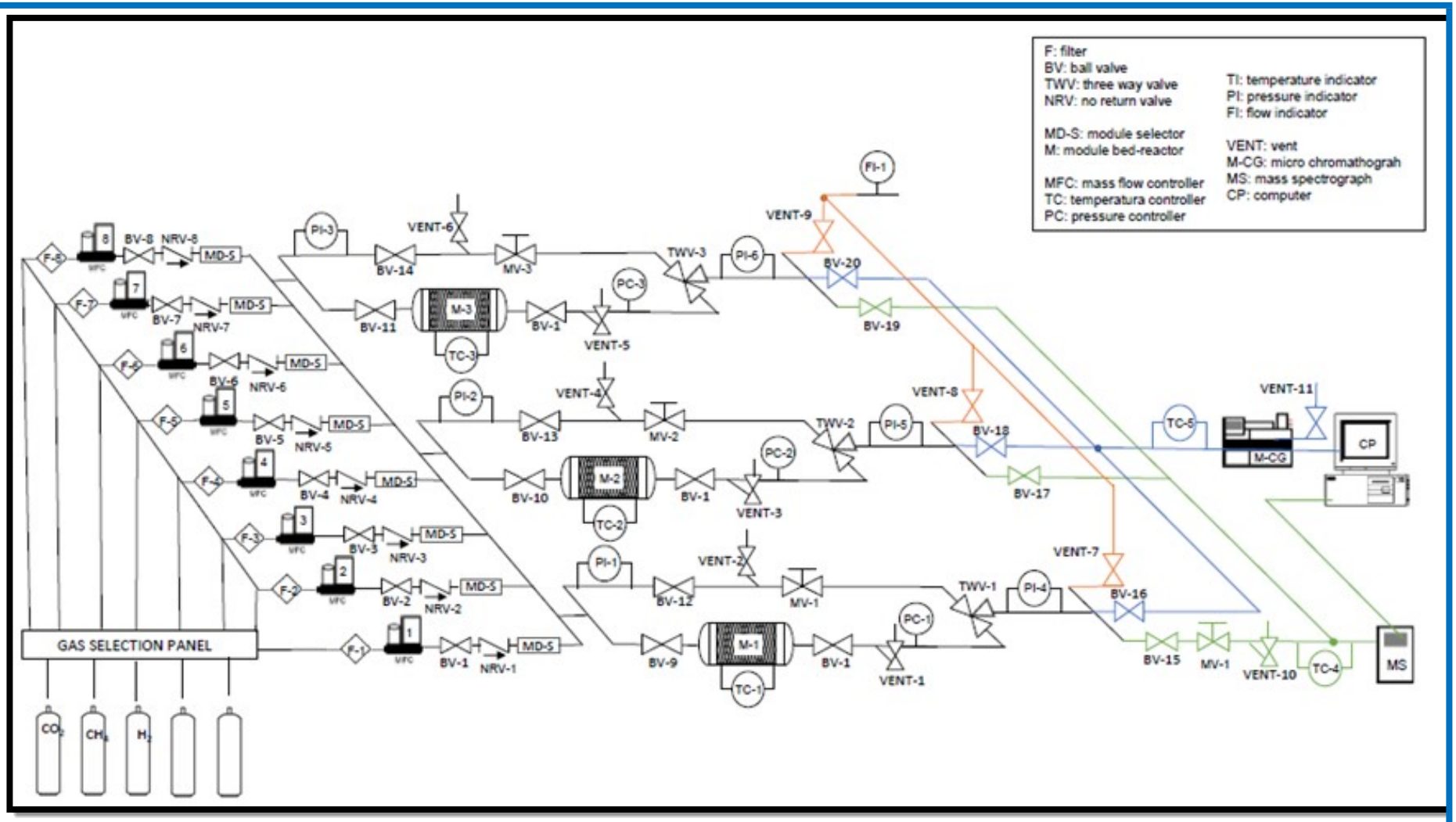

Figure S11.
Schematic diagram of the experimental set-up used for the breakthrough experiments. The fixed bed column is highlighted with dashed red line.

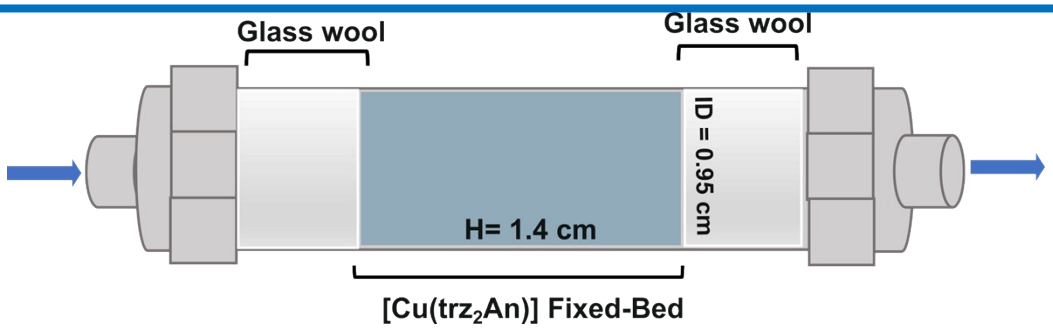

Figure S12. Column packing configuration for [Cu(trz_2An)] powder.

Supplementary Text ST1

Possible metal leaching from aqueous [Cu(trz_2An)] suspensions was tested as follows. After soaking three samples (15.0 mg each one) of [Cu(trz_2An)] crystals in 10 mL of MilliQ water at pH 3, 7 and 10 (the pH of which was changed thanks to a few drops of diluted HCl and/or NaOH solutions) for 20 hours, the amount of copper ions release was verified by quantitative ICP-OES measurements on the filtered aqueous solutions. The ICP-OES analysis was conducted on a 5110 Agilent spectrometer by monitoring all Cu emission lines simultaneously. Standard solutions were prepared in a 1-100 mg L^{-1} concentration range starting from certified solutions with Cu concentrations of 99.77±0.32 mg kg^{-1} and 9559±73 mg kg^{-1}. The obtained results are summarized in Table ST1. The values of Cu^{II} ion concentration were computed as the average and standard deviation (±σ) of the values obtained for the different emission lines. Based on the observed values, we conclude that metal leaching is negligible and that [Cu(trz_2An)] is stable under the entire range of pH investigated.

Table ST1. Results of ICP-OES analyses, confirming that no significant metal leaching occurs by suspending [Cu(trz_2An)] in neutral, acidic and basic conditions.

pH	Cu(II) concentration (mg L^{-1})
3.02	0.03±0.01
6.98	0.01±0.01
9.92	0.03±0.01

Supplementary Text ST2

In order to test the reproducibility of our synthetic protocol, and in the light of the observed precipitation of distinct, but similar, monoclinic *vs.* orthorhombic crystal phases, we have performed *five times* the synthesis and isolation of the polyhydrated [Cu(trz_2An)] solid material using the same procedure, described hereafter. XRD patterns, synoptically illustrated in Figure ST2, are similar, but, subjected to a structureless whole-pattern profile fitting procedure of the Pawley type (*J. Appl. Cryst*., **1981**, *14*, 357), provided statistically different cell values, inserted in Table ST2. This nicely demonstrates the partial flexibility of the whole framework and the occasional symmetry shift from monoclinic ($\beta \neq 90°$) to orthorhombic ($\beta = 90°$), though this little change hardly modifies material performance.

Synthetic protocol:

$CuCl_2 \cdot 2H_2O$ has been slowly added to an aqueous solution containing the H_2trz_2An ligand and NaOH in 1:1:2 molar ratios. The final mixture was heated in a sealed autoclave under hydrothermal conditions at 140°C for 54 hours. Brown powders were isolated upon cooling and were washed three times by using a mildly acidic (pH = 5) HCl solution capable of solubilizing residual $Cu(OH)_2$.

Supplementary Text ST2 (cont'd)

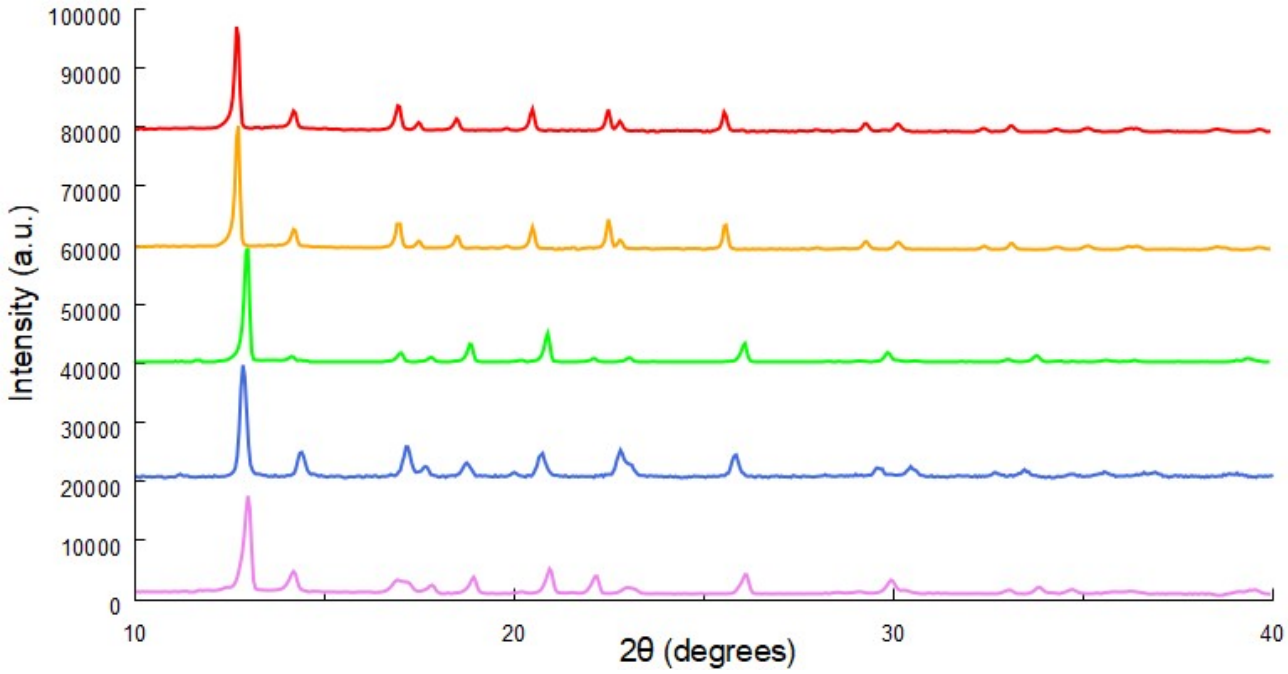

Figure ST2. Test of reproducibility of XRD patterns upon repeating five times the synthetic protocol described above (bottom to top: Preparations 1 to 5). The cell parameters and crystal system are reported in Table ST2.

Table ST2. Cell parameters obtained after Pawley refinement, demonstrating the flexibility of the [Cu(trz_2An)] crystal phase. Typical esd's are in the third decimal digit for a, b and c, and in the second decimal digit for monoclinic β angle. Cell volumes, normalized by the Z = 2 value, are rounded to the closest integer value.

Preparation	a, Å	b, Å	c, Å	β, °	V/Z, Å^3	Crystal System
1	9.406	9.977	8.048	91.28	378	Monoclinic
2	9.514	10.094	7.832	90	376	Orthorhombic[a]
3	9.430	9.962	8.069	90	379	Orthorhombic[a]
4	9.603	10.154	7.919	90	386	Orthorhombic[a]
5	9.606	10.153	7.918	90	386	Orthorhombic[a]

[a] no superstructure peaks, such as those observed in the single-crystal analysis of the orthorhombic form with doubled **b** axis, were observed.

Supplementary Text ST3.

Here we propose the details of the comparative geometrical analysis of the porosity of the [Cu(trz_2An)] and [Co(trz_2An)] structures, where the cavities illustrated in Figure 4 are idealized by an elliptical cylinder, in line with what previously reported.The descriptors used are:

- the major axis of the ellipsoid (*c*) is taken as the distance H1···H1 in [Cu(trz_2An)] and H8···H8 in [Co(trz_2An)].

- the minor axis (*b*) is taken as the maximum pore diameter calculated by the size of the largest sphere that can fit into the cavity.

- the volume (V_p) is equal to half that calculated in a unit cell (probe radius: 1.20 Å; space grid:0.30 Å).

- the major axis (*a*) is derived from the other parameters.

Regarding the size of the CO_2 molecule, it has recently been highlighted that a simple description that only takes into account the kinetic diameter (D_k, a scalar value) is not sufficient to explain its diffusion and, in general, that of polyatomic gas molecules in porous solids. In fact, the molecule is linear ($D_{\infty h}$ symmetry) and is best described by two types of dimensions, one transversal and one longitudinal, approximating a cylinder. [1,2]These diameters may vary slightly depending on how they are calculated,[2] but it is generally accepted that the transverse diameter is equal to D_k, while its length is considered to be equal to the O…O distance of 2.32 Å, augmented by twice the Van der Waals radius of O $r_{VdW,O}$ = 1.52 Å, reaching ca. 5.4 Å (the standard r_{VdW} value predent in Olex and Mercury were used). [1–5] Considering the cylindrical shape of the pores, and that they have a minor axis *b* that is almost equal to $D_k(CO_2)$ = 3.30 Å, (therefore blocking CO_2 in this dimension), the problem reduces to positioning two ovals that describe the longitudinal cross-section of CO_2 within the rectangular section of the cylinder described by the *ac* plane. Our crude geometrical analysis, portrayed in Figure ST3, shows that in the *m*-[Cu(trz_2An)] crystal phase, the presence of two CO_2 molecules appears less likely, as they may overlap. At variance, two CO_2 molecules seem to fit perfectly into the [Co(trz_2An)] cavity. Whether this is the true reason for the lower adsorption capacity of the Cu-, vs. Co-based crystal phase, we cannot guarantee. Indeed, cavity merging promoting gas permeation and other dynamical effects must be at work, partially limiting the validity of this purely geometric (thus, static) analysis.

References **Supplementary Text ST3**

1 S. Kunze, R. Groll, B. Besser and J. Thöming, *Sci. Rep.*, 2022, **12**, 2057.

2 J. Wang, Y. Zhang, W. Wang, L. Yin, M. Xie, J. Y. Lee, H. Shi and H. Liu, *J. Phys. Chem. A*, 2023, **127**, 517–526.

3 N. Mehio, S. Dai and D. Jiang, *J. Phys. Chem. A*, 2014, **118**, 1150–1154.

4 S. Geng, H. Xu, C. Cao, T. Pham, B. Zhao and Z. Zhang, *Angew. Chemie Int. Ed.*, ,

5 H. Sakamoto, K. Otake and S. Kitagawa, *Commun. Mater.*, 2024, **5**, 17

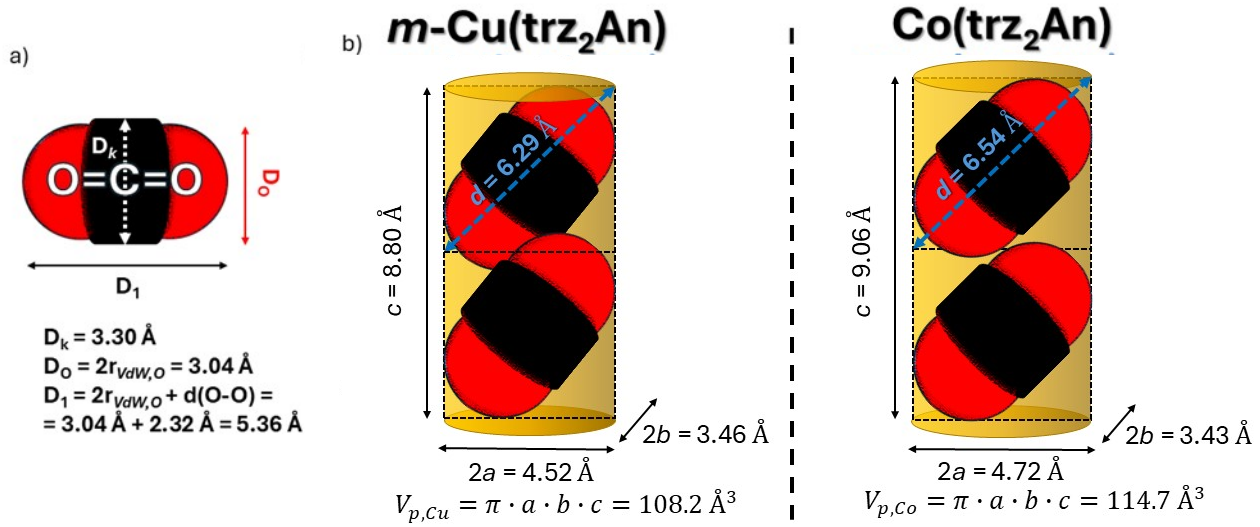

Figure ST3. Illustration of the geometrical analysis described above and in Table S2. a) idealized geometrical parameters for a static and isolated CO_2 molecule. b) A 2D representation of the model described in the ST3 text for cavities approximated by elliptical cylinders of *m*-[Cu(trz$_2$An)] and [Co(trz$_2$An)] hosting two CO_2 molecules each. D_o = Van der Waals radius for Oxygen; D_k = CO_2 kinetic diameter; D_1 =CO_2 length; V_p = volume of one cavity; *a* = major semi-axis of the elliptical cylinder; *b* = minor semi-axis of the elliptical cylinder; *c* = cylinder length; *d* = diagonal of half *ac* plane. The diagonal of the rectangle that ideally fits the dimensions of CO_2 *d*=6.62 Å was calculated as shown in Panel b.

Supplementary Text ST4. Thermal characterization from VT-XRD analysis.

Strain tensor calculation (Bilbao Crystallographic Server app), www.cryst.ehu.es/cryst/strain.html, based on Ohashi. Y., and Burnham. C.W. *American Mineral.*, 1973, **58**, 843–849.

```
Strain tensor calculation
Lattice parameters of cell number 1 (undeformed):     (25˚C)
9.4100 9.9700 8.0400 90.000 91.400 90.000
Lattice parameters of cell number 2 (deformed):       (115˚C)
9.0500 10.2300 8.0400 90.000 96.000 90.000

Metric tensor M1:
[  88.548100  0.000000 -1.848451 ]
[  0.000000  99.400900  0.000000 ]
[ -1.848451  0.000000  64.641600 ]

Metric tensor M2:

[  81.902500  0.000000 -7.605700 ]
[  0.000000  104.652900  0.000000 ]
[ -7.605700  0.000000  64.641600 ]

Standard root tensor R1:

[  9.407191  0.000000  0.000000 ]
[  0.000000  9.970000  0.000000 ]
[ -0.229907  0.000000  8.040000 ]

Standard root tensor R2:

[  9.000423  0.000000  0.000000 ]
[  0.000000  10.230000  0.000000 ]
[ -0.945983  0.000000  8.040000 ]

Note: The standard root tensor R of metric tensor M=RTR transforms fractional direct space
coordinates X, into cartesian coordinates Xc such: Xc = R X
Linear Lagrangian Strain Tensor (small deformation)

[ -0.043240 -0.000000 -0.038060 ]
[ -0.000000  0.026078  0.000000 ]
[ -0.038060  0.000000  0.000000 ]

Eigenvalues: 0.02608 -0.06539 0.02215

Note: The linear Lagrangian strain tensor can be calculated according to the formula: S = 0.5
(e + eT), where, e = R2R1-1 - I and, R1 and R2 are the standard root tensors of cell 1 and 2,
and I is a 3x3 identity matrix

Finite Lagrangian Strain Tensor (finite deformation)

[ -0.039408 -0.000000 -0.038060 ]
[ -0.000000  0.026418  0.000000 ]
[ -0.038060  0.000000  0.000000 ]

Eigenvalues: 0.02642 -0.06256 0.02315

Degree of lattice distortion: 0.02392

Note: The finite Lagrangian strain tensor can be calculated according to the formula: S = 0.5
(e + eT + eT e), where, e = R2R1-1 - I and, R1 and R2 are the standard root tensors of cell 1
and 2, and I is a 3x3 identity matrix
```

Note: The degree of lattice distortion is described here as the spontaneous strain (square root of the sum of squared eigenvalues of strain tensor) divided by 3

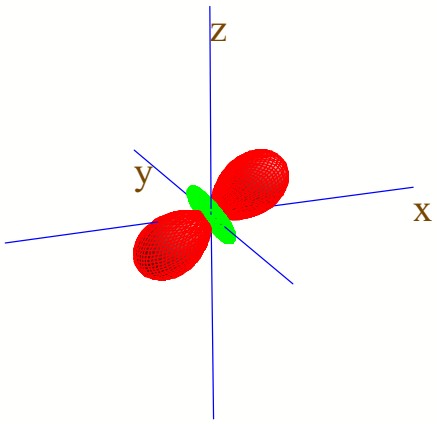

Figure ST4. Visualization of the Finite Lagrangian Strain Tensor, performed by Wintensor (Kaminsky, P.M.W.; Snyder, T.; Stone-Sundberg, J., *Zeit. Krist., Cryst. Mater.*, 2015, **230**, 651–656; see also cad4.cpac.washington.edu/WinTensorhome/WinTensor.htm). Positive/negative values in green and red.

Linear and volumetric thermal expansion values are calculated, in the 25-115°C range, as

$\kappa_x = [(x_{115°C} - x_{25°C})/x_{25°C}]/(115\text{-}25)$, for x = a, b, c, β and V.

κ_a = -430 MK^{-1}, κ_b = +29 MK^{-1}, $|\kappa_c| \leq 10$ MK^{-1}, κ_β = 559 MK^{-1}, κ_V = -180 MK^{-1}

Table S1. Porosity parameters calculated using the Pore Analyser Tool (in Mercury) for the two polymorphic forms of "dehydrated" [Cu(trz_2An)].

Parameter	Monoclinic	Orthorhombic	Unit
System Volume	751.7	1495.9	Å³
System Mass	671.4	1342.9	g/mol
System Density	1.483	1.491	g/cm³
Void Volume[a]	28.8	27.6	%
Total surface area	0	0	Å²
Total surface area per volume	0	0	m²/cm³
Total surface area per mass	0	0	m²/g
Network-accessible surface area	0	0	Å²
Network-accessible surface area per volume	0	0	m²/cm³
Network-accessible surface area per mass	0	0	m²/g
Total helium volume	199.377	345.1	Å³
Total helium volume	0.179	0.155	cm³/g
Total geometric volume	330.884	663.0	Å³
Total geometric volume	0.297	0.297	cm³/g
Network-accessible helium volume	199.377	345.1	Å³
Network-accessible helium volume	0.179	0.155	cm³/g
Network-accessible geometric volume	330.744	662.7	Å³
Network-accessible geometric volume	0.297	0.297	cm³/g
Pore limiting diameter	1.73	2.01	Å
Maximum pore diameter	3.46	3.29	Å

[a] probe radius: 1.2 Å; grid spacing: 0.3 Å

Table S2. Comparative porosity parameters derived geometrically using the elliptical cylinder model discussed in ST3, for both "dehydrated" [Cu(trz_2An)] (*m*- form) and [Cu(trz_2An)] phases.

Parameter	*m*-[Cu(trz_2An)]	[Co(trz_2An)]	Unit
Single 0D Cavity Volume (V= πabc)	108.2	114.7	Å^3
Cylinder height (c)	8.80	9.06	Å
Elliptical base short axis (b)	1.73	1.72	Å
Elliptical base long axis (a = V/πbc)	4.528	4.72	Å
$D_0 = r_{vdW,O}$	CO_2 molecule	1.52	Å
d(O-O)	CO_2 molecule	2.32	Å
$D_1 = 2\ D_0 + d(O\text{-}O)$	CO_2 molecule	5.36	Å
d (see Figure ST3)	6.29	6.62	Å

Table S3. Breakthrough experimental adsorption data for various gas ratios in N_2/CO_2 and CH_4/CO_2 mixtures.

P (bar)	T (K)	F_{N2} (NmL min^{-1})	F_{CO2} (NmL min^{-1})	F_{CH4} (NmL min^{-1})	F_t (NmL min^{-1})	C_{N2} (%)	C_{CO2} (%)	C_{CH4} (%)	Bt (min g^{-1})	CO_2 q_b (mmol g^{-1})	CO_2 q_s (mmol g^{-1})	CH_4 q_s (mmol g^{-1})	N_2 q_s (mmol g^{-1})	αs CO_2/N_2	αs CO_2/CH_4
1.05	298	7.5	7.5	-	15	50	50	0	2.6	0.79	1.63	-	0.38	4.3	-
1.05	298	13	2	-	15	80	20	0	2.7	0.33	0.95	-	0.49	7.8	-
1.05	298	14.3	0.75	-	15	95	5	0	2.5	0.08	0.27	-	0.63	8.1	-
1.05	298	7.5	7.5	-	15	50	50	0	2.5	0.77	1.62	-	0.4	4.1	-
1.05	298	7.5	7.5	-	15	50	50	0	2.6	0.8	1.67	-	0.41	4.1	-
1.05	298	0	7.5	7.5	15	0	50	50	2.5	0.76	1.69	0.42	-	-	4.0
1.05	298	0	7.5	7.5	15	0	50	50	2.4	0.73	1.65	0.37	-	-	4.5
1.05	298	0	7.5	7.5	15	0	50	50	2.5	0.74	1.64	0.37	-	-	4.4
1.05	298	7.5*	7.5*	-	15*	49.1	49.1	0	2.2	0.71	1.81	-	0.49	3.7	-
1.05	298	7.5*	7.5*	-	15*	49.1	49.1	0	1.8	0.6	1.81	-	0.47	3.9	-
1.05	298	7.5*	7.5*	-	15*	49.1	49.1	0	2.3	0.81	1.86	-	0.32	5.8	-
1.05	298	7.5*	7.5*	-	15*	49.1	49.1	0	2.2	0.81	1.66	-	0.35	4.7	-
1.05	298	7.5*	7.5*	-	15*	49.1	49.1	0	1.7	0.6	1.79	-	0.53	3.4	-

**Experiments under controlled humid conditions, dew point = 15 °C, corresponding water vapor mole fraction of 1.67% (~53% RH at 1bar and 25°C). Separation performance of [Cu(trz$_2$An)] (0.87 g activated) for N_2/CO_2 and CH_4/CO_2 gas mixtures at different gas compositions ratios. CO_2 adsorption capacities at breakthrough (q_b) were evaluated at C/C_o = 0.05. q_s refers to the CO_2 adsorption capacity at saturation point (C/Co = 1). All experiments used helium as carrier gas (30 mL/min) and a inline micro-GC for outlet gas concentration analysis. "α_s" refers to the Selectivity at saturation point.*

Table S4. Crystal data and structure refinement for *o*-Cu(trz_2An)·$3H_2O$

Empirical formula	$C_{10}H_{10}CuN_6O_7$
Formula weight	389.78
Temperature/K	100(2)
Crystal system	Orthorhombic
Space group	$P2_1nb$
a/Å	9.4793(8)
b/Å	19.6950(15))
c/Å	8.0125(6)
α/°	90
β/°	90
γ/°	90
Volume/Å^3	1495.9(2)
Z	4
ρ_{calc}g/cm^3	1.731
μ/mm^{-1}	1.510
F(000)	788.0
Crystal size/mm^3	0.25 × 0.16 × 0.06
Radiation	MoKα (λ = 0.71073)
2Θ range for data collection/°	4.136 to 55.524
Index ranges	-12 ≤ h ≤ 12, -25 ≤ k ≤ 25, -10 ≤ l ≤ 10
Reflections collected	52143
Independent reflections	3536 [R_{int} = 0.0794, R_{sigma} = 0.0303]
Data/restraints/parameters	3536/0/217
Goodness-of-fit on F^2	1.113
Final R indexes [I>=2σ (I)]	R_1 = 0.0453, wR_2 = 0.1114
Final R indexes [all data]	R_1 = 0.0499, wR_2 = 0.1136
Largest diff. peak/hole / e Å^{-3}	0.85/-0.56
Flack parameter	0.49(3)

Table S5. CO_2/CH_4 (50:50) and CO_2/N_2 (50:50) separation performance of selected MOFs (1 bar, 298 K).

MOF	CO_2 adsorption capacity in mixed (50:50) gas phase (mmol g^{-1})	CO_2/CH_4 ideal selectivity	CO_2/N_2 ideal selectivity	BET surface area (m^2 g^{-1})	References
CuMOF	1.65	4.50[b]	>100 (4.1[b])	…	This work
CoMOF	1.7	>1000	>1000	431	6
MUF-16	1.81	6686.00	36.2	214	7
Qc-5-Cu-sql-B	1.61	3300.00	4000	222	8,9
USTA-16	4.25[a]	105.00[a]	15.6[a]	628	10
5a	2.50	59.30		230	11
Zn4O(L)2	2.35	41.20		10.7	12
Zn2(L)	1.00	39.00		240	13
UTSA-49	1.31	33.70		710.5	14
TAMOF-1	3.16	32.80		980	15
MgMOF-74	4.8	12	26	1640	16,17
1·S	0.75	28.60		493	18
IITKGP-5	1.83	23.80		336	19
Zn14(L)6	1.00	22.50		389.6	16
MAF-X7	0.84	22.00		--	20
Cu2(L)	0.75	6.80		1860	21
HKUST-1	2.4	10	29.1	1317	22

[a] Measured at 2 bar and 298K.

[b] Experimental dynamic selectivity (α)

References for Table S5

6 N. Monni, E. Andres-Garcia, K. Caamaño, V. García-López, J. M. Clemente-Juan, M. Giménez-Marqués, M. Oggianu, E. Cadoni, G. Mínguez Espallargas, M. Clemente-León, M. L. Mercuri and E. Coronado, *J. Mater. Chem. A*, 2021, **9**, 25189–25195.

7 O. T. Qazvini, R. Babarao and S. G. Telfer, *Nat. Commun.*, 2021, **12**, 197.

8 K. Chen, D. G. Madden, T. Pham, K. A. Forrest, A. Kumar, Q. Yang, W. Xue, B. Space, J. J. Perry, J. Zhang, X. Chen and M. J. Zaworotko, *Angew. Chemie Int. Ed.*, 2016, **55**, 10268–10272.

9 R.-B. Lin, S. Xiang, W. Zhou and B. Chen, *Chem*, 2020, **6**, 337–363.

10 S. Xiang, Y. He, Z. Zhang, H. Wu, W. Zhou, R. Krishna and B. Chen, *Nat. Commun.*, 2012, **3**, 954.

11 Y.-H. Chai, Y. Zhao, X.-Y. Liu, Z.-Y. Cui, B.-T. Zhao and L.-F. Ma, *Cryst. Growth Des.*, 2022, **22**, 5559–5570.

12 Y. Zhao, L. Wang, N.-N. Fan, M.-L. Han, G.-P. Yang and L.-F. Ma, *Cryst. Growth Des.*, 2018, **18**, 7114–7121.

13 B. Liu, W.-P. Wu, L. Hou, Z.-S. Li and Y.-Y. Wang, *Inorg. Chem.*, 2015, **54**, 8937–8942.

14 S. Xiong, Y. Gong, H. Wang, H. Wang, Q. Liu, M. Gu, X. Wang, B. Chen and Z. Wang, *Chem. Commun.*, 2014, **50**, 12101–12104.

15 S. Capelo-Avilés, M. de Fez-Febré, S. R. G. Balestra, J. Cabezas-Giménez, R. Tomazini de Oliveira, I. I. Gallo Stampino, A. Vidal-Ferran, J. González-Cobos, V. Lillo, O. Fabelo, E. C. Escudero-Adán, L. R. Falvello, J. B. Parra, P. Rumori, G. Turnes Palomino, C. Palomino Cabello, S. Giancola, S. Calero and J. R. Galán-Mascarós, *Nat. Commun.*, 2025, **16**, 3243.

16 Z. Bao, L. Yu, Q. Ren, X. Lu and S. Deng, *J. Colloid Interface Sci.*, 2011, **353**, 549–556.

17 X. Zhang, Q. Zheng and H. He, *Microporous Mesoporous Mater.*, 2022, **336**, 111899.

18 Y.-P. Zhao, Y. Li, C.-Y. Cui, Y. Xiao, R. Li, S.-H. Wang, F.-K. Zheng and G.-C. Guo, *Inorg. Chem.*, 2016, **55**, 7335–7340.

19 A. Pal, S. Chand, S. M. Elahi and M. C. Das, *Dalt. Trans.*, 2017, **46**, 15280–15286.

20 J.-B. Lin, W. Xue, J.-P. Zhang and X.-M. Chen, *Chem. Commun.*, 2011, **47**, 926–928.

21 B. Liu, H.-F. Zhou, L. Hou, Z. Zhu and Y.-Y. Wang, *Inorg. Chem. Front.*, 2016, **3**, 1326–1331.

22 M. He, F. Xia, T. Xu, X. Gao, Z. Jiang, X. Wang and Y. He, *Dalt. Trans.*, 2019, **48**, 11374–11381.